Faraday Discussions

Accepted Manuscript

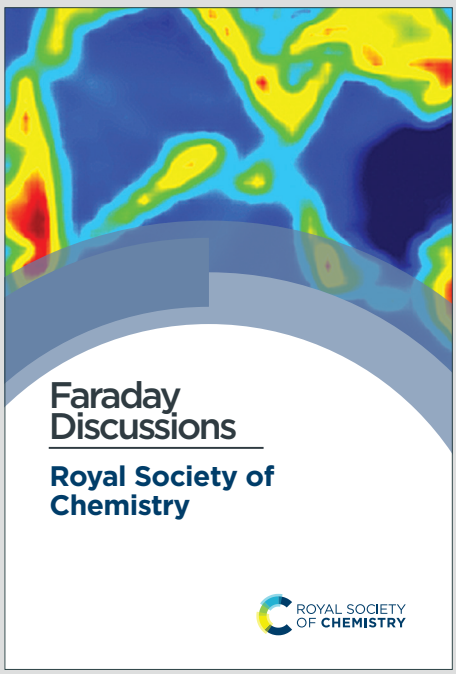

This article can be cited before page numbers have been issued, to do this please use: R. Kanemoto, A. Bashkatov, S. Park, J. A. Wood, M. T.M. Koper, D. Lohse and D. Krug, *Faraday Discuss.*, 2026, DOI: 10.1039/D6FD00106H.

ROYAL SOCIETY OF CHEMISTRY

www.rsc.org/faraday_d

View Article Online
DOI: 10.1039/D6FD00106H

Electrocatalytic performance enhancement through coalescence-induced bubble dynamics: the case of the anode†

Ryo Kanemoto,[a] Aleksandr Bashkatov,*[a] Sunghak Park,[b] Jeffery A. Wood,[c] Marc T.M. Koper,[d] Detlef Lohse[e,f] and Dominik Krug[a,e]

Received 00th 00 20xx, Accepted 00th 00 20xx DOI: 10.1039/x0xx00000x

Electrolytically generated hydrogen and oxygen bubbles can substantially reduce the efficiency of (water) electrolysis by blocking active electrode area and increasing ohmic losses. There is therefore an interest in strategies to improve bubble removal, particularly under microgravity where buoyancy, which favors bubble departure under terrestrial conditions, is absent. Both in alkaline and acidic electrolytes, O_2 bubbles tend to remain at the electrode for longer, in part due to solutal Marangoni effects, and detach at significantly larger sizes compared to H_2 bubbles. As an alternative to buoyancy-driven removal, coalescence between a pair of bubbles can induce bubble detachment from the electrode and is therefore a highly attractive mechanism. Building on our previous work demonstrating that coalescence-induced H_2 bubble departure can enhance electrochemical performance using a dual Pt microelectrode system, we now extend this approach to the oxygen evolution reaction in $HClO_4$, KOH and H_2SO_4. By combining high-speed imaging with electrochemical measurements, we show that coalescence can trigger substantially earlier O_2 bubble departure as compared to buoyancy effects alone, reducing the anodic overpotential by up to ∼100-200 mV under galvanostatic conditions, which is equivalent to an enhancement of the reaction current by up to a factor of ≈ 2 under potentiostatic conditions. Earlier bubble departure also enables stable operation at substantially higher currents that would otherwise be limited by the bubbles blocking the electrode surface. At elevated currents, however, we find that coalescence between neighbouring bubbles becomes progressively inhibited and delayed, leading to larger detachment size and eventually preventing the formation of a single bubble beyond ≈ 1 mA. Finally, in contrast to previous observations for H_2 in H_2SO_4, our data shows that once departed, O_2 bubbles are unlikely to return to the electrode via repeated near-electrode coalescence. We attribute this contrast between O_2 and H_2 bubbles to the inherently lower O_2 gas production rate, which is half that of H_2 at a fixed current.

Introduction

Water electrolysis is a cornerstone technology for a future CO_2-neutral energy system, as it allows electrical energy from renewable energy sources such as wind and solar to be transformed into chemical energy in the form of hydrogen, which can then be stored and transported [1]. The hydrogen produced is relevant not only as a fuel and energy carrier [2], but in particular also as a feedstock for fertilizer (ammonia) production, direct reduction of iron in steel production (coal replacement), and the synthesis of hydrocarbons, synthetic fuels, and other chemicals [3]. Water electrolysis is also an essential process for space applications, where it can provide a sustainable source of oxygen for life support, for example, on the International Space Station (ISS) [4]. At the same time, hydrogen can be reacted with CO_2 to generate water and reduced carbon products via Sabatier or Bosch reactions, forming a key element of in-situ resource utilization (ISRU) [5]. During water electrolysis, however, hydrogen and oxygen gas bubbles form at the electrocatalytic surfaces [6]. These gas phases are non-conductive and thus raise ohmic resistance by blocking the ion-conducting pathways [7]. Additionally, they mask the active area of the electrodes and reduce the number of available reaction sites. Consequently, a considerable part of the overpotential can be attributed to the presence of H_2 and O_2 bubbles at the electrode surface and in the electrolyte bulk [8]. Enhanced removal of gas bubbles is therefore essential to minimize overpotentials [6,9] and enable stable operation at high current densities, in both conventional alkaline and proton exchange membrane water electrolyzers.

A variety of active methods, such as sonication [10], forced convection [11,12], and magnetic polarization [13,14], have been proposed and tested to accelerate bubble removal from catalytic surfaces [15]. Although such techniques can be highly effective, passive methods are particularly attractive because they do not require an external energy input. For example, hydrophilic surfaces, in general, promote bubble detachment by reducing the contact angle at liquid-solid interface [16]. At the same time, bubble removal can also benefit from hydrophobic surfaces. A promising example is bubble-free electrolysis based on gas-diffusion electrodes, where the produced gas (dissolved) is continuously extracted through a hydrophobic porous network, often made of expanded PTFE, into a connected gas chamber without bubble formation [17,18]. In practice, however, entirely bubble-free operation is typically limited to relatively low current densities [18–20].

Another passive approach is surface patterning of the catalyst to control the preferred location of bubble nucleation. This can be achieved, for example, through laser structuring [21] or by depositing hydrophobic fractions, such as PTFE spots, on the electrode surface. In the latter, produced gas migrates away from the active electrode area toward the hydrophobic regions [22,23], where bubble nucleation preferentially occurs, thus potentially reducing bubble-induced overpotentials [24,25]. In addition, densely packed Pt-coated micropost arrays [26] or gold strip arrays [27] have been demonstrated to promote the release of smaller bubbles through their mutual coalescence. In

[0a] Institute of Aerodynamics, RWTH Aachen University, Wüllnerstraße 5a, 52062 Aachen, Germany. E-mail: a.bashkatov@aia.rwth-aachen.de
[0b] Department of Future Energy Engineering, Sungkyunkwan University (SKKU), Suwon 16419, Republic of Korea.
[0c] Soft Matter, Fluidics and Interfaces, MESA+ Institute for Nanotechnology, J. M. Burgers Centre for Fluid Dynamics, University of Twente, Enschede 7500 AE, Netherlands.
[0d] Leiden Institute of Chemistry, Leiden University, Leiden 2300 RA, The Netherlands.
[0e] Physics of Fluids Group, Max Planck Center for Complex Fluid Dynamics and J. M. Burgers Centre for Fluid Dynamics, University of Twente, Enschede 7500 AE, Netherlands.
[0f] Max Planck Institute for Dynamics and Self-Organization, Göttingen 37077, Germany.
[0†] Supplementary Information available: [details of any supplementary information available should be included here]. See DOI: 00.0000/00000000.

View Article Online
DOI: 10.1039/D6FD00106H

case the released surface energy during this process is sufficient to overcome viscous dissipation and adhesion energy, coalescence can lead to bubble departure independent of buoyancy[28]. This removal mechanism is particularly attractive not only under terrestrial conditions, but also in microgravity environment, where the near-absence of buoyancy severely hinders phase separation and makes bubble detachment and removal much more difficult than on Earth[4,29].

Recent studies have shown that coalescence-induced dynamics of electrogenerated gas bubbles can be exploited to improve the performance of gas-evolving electrodes. In our previous work[30], using a dual ∅100 μm microelectrode system with an interelectrode distance H varied from 117 μm to 270 μm, we demonstrated that, depending on the applied potential (ϕ), coalescence-induced detachment can increase the mean current by a factor of ≈ 2.4-fold during hydrogen evolution reaction (HER) in H_2SO_4 compared with buoyancy-driven departure at a single microelectrode. On the other hand, beyond a critical current repeated coalescence with bubbles forming near the electrode can drive a previously departed bubble back toward the surface, where it is held between the two microelectrodes by thermal[31–33] and solutal[34–36] Marangoni forces. This leads to the resumption of bubble growth with the bubble located in between the electrodes, preventing the formation of larger bubbles directly on the electrodes, followed by buoyancy-driven departure. Consequently, this regime was also found to be beneficial, especially at larger interelectrode distances H. It was also shown that at low potentials the dual electrode can perform worse than a single electrode. Under these conditions, bubbles grow slowly, and the combined electrode masking by the two bubbles, together with the diffusive competition between the two reaction sites, can outweigh the benefits of coalescence-induced detachment.

More recently, Zhang *et al.*[37] extended the explored range of interelectrode distances up to $H = 1489$ μm and reported similar performance enhancement during HER, reaching up to a ≈ 2.5-fold increase at $H = 262$ μm (see Fig. S6 in Supporting Information[37]). They further concluded that the optimal H, where performance peaks, increases with increasing potential and decreasing electrode size. Consistent with these findings, Zhao *et al.*[38] reported similar performance enhancements for both horizontal (up to a ≈ 2.1-fold increase) and vertical (up to a ≈ 1.5-fold increase) electrode configurations at $H = 260$ μm. In contrast, Lu *et al.*[39] reported that dual microelectrode with $H = 800$ μm reduces the performance by a factor of ≈ 1.3 relative to a single electrode, which they largely attributed to the elevated ohmic resistance associated with dual electrode operation at such large interelectrode spacing. Finally, Yang *et al.*[40] extended this concept to O_2 bubbles in alkaline electrolyte (KOH) and showed that optimal spacing shifts from $H = 112$ μm at $\phi = 2.6$ V to $H = 185$ μm at $\phi \geq 3.0$ V (vs. RHE). Although the enhancement relative to a single electrode was not quantified explicitly, the dual electrode consistently demonstrated larger mean currents.

Despite these recent advances, the current understanding of bubble dynamics, in particular coalescence-induced dynamics, remains largely based on HER, while considerably less attention has been devoted to O_2 bubbles during OER. Because of the fundamentally different local environment at the cathode and anode, models and design strategies derived primarily from H_2 bubble studies may not directly apply to O_2 bubbles. In particular, O_2 bubbles tend to remain at the electrode for longer and to be larger than H_2 bubbles, especially in alkaline electrolytes[41–45], pointing to substantial variations in the underlying force balance. Although recent studies have partially rationalized these differences through Marangoni effects[35,36], which depend on both the reaction and electrolyte composition, a comprehensive mechanistic understanding of O_2 bubble dynamics at microelectrodes remains elusive. This problem is particularly relevant because OER constitutes a major electrochemical bottleneck due to its four-electron-transfer mechanism.

In the present work, we extend our previous study on the coalescence-induced dynamics of H_2 bubbles in H_2SO_4[30] to O_2 bubble evolution at dual microelectrodes in both acidic and alkaline electrolytes, using a single microelectrode as a benchmark. We show that O_2 bubbles at a single microelectrode are generally characterized by larger detachment sizes and lifetimes exceeding those of H_2 bubbles in H_2SO_4 by more than an order of magnitude. Consequently, coalescence-induced detachment in the dual microelectrode configuration, reducing both the detachment size and lifetime, is beneficial and thus reduces the anodic overpotential by up to ≈ 100-200 mV under galvanostatic conditions and enhances the reaction rate by up to a factor of ≈ 2 under potentiostatic conditions, relative to buoyancy-driven detachment at a single microelectrode.

This paper is organized as follows. The *Methods* section describes the experimental setup and procedures. The *Results and Discussion* section introduces O_2 bubble dynamics in single and dual microelectrode systems, quantifies the performance benefits of coalescence-induced premature detachment, enabled by dual microelectrode, as a function of applied current [potential], electrolyte composition, and interelectrode distance, and discusses coalescence inhibition at high currents. Finally, the *Conclusions* section summarizes our key findings and discusses implications for related systems.

Methods

The experimental approach closely resembles that used in our previous study on coalescence-induced dynamics of H_2 bubbles[30]. O_2 bubbles were generated during water electrolysis on the dual microelectrode serving as the working electrode in a three-electrode electrochemical cell, shown in Fig. 1. The dual microelectrode consists of two Pt wires (99.99%, ∅100 μm each) separated from each other by interelectrode distance H and sealed into a soda-lime glass capillary, such that only their cross-sections are exposed to the electrolyte. Each wire has an independent electrical connection, allowing the two electrodes to be operated separately. This enabled, for example, operation of only a single electrode, which served as a baseline case in the present work. The electrode surface was polished using 2000 grit sandpaper, sonicated for 10 minutes, and rinsed with ultrapure water (≥18.2 MΩ cm) prior to each set of measurements. The working electrode is inserted from the bottom of a transparent glass cuvette (with a 10 mm × 10 mm cross-section and a height of 40 mm) filled with 0.5 M $HClO_4$, 0.5 M KOH or 0.5 M H_2SO_4, providing a horizontal orientation for the active electrode area. These electrolytes were selected to investigate the influence of electrolyte composition on O_2 bubble dynamics. In particular, $HClO_4$ and KOH are expected to exhibit qualitatively similar bubble dynamics owing to the same direction of the solutal Marangoni force despite their contrasting pH values, whereas H_2SO_4 is expected to behave differently even though its pH is comparable to that of $HClO_4$[35], because the solutal Marangoni force points in the opposite direction. The electrochemical cell is completed by the counter electrode (Pt wire, 99.99%, ∅0.5 mm) and an Ag/AgCl reference electrode, both inserted from the top of the glass cuvette, and connected to an electrochemical workstation (BioLogic

View Article Online
DOI: 10.1039/D6FD00106H

or OrigaLys) operated either under galvanostatic or potentiostatic conditions.

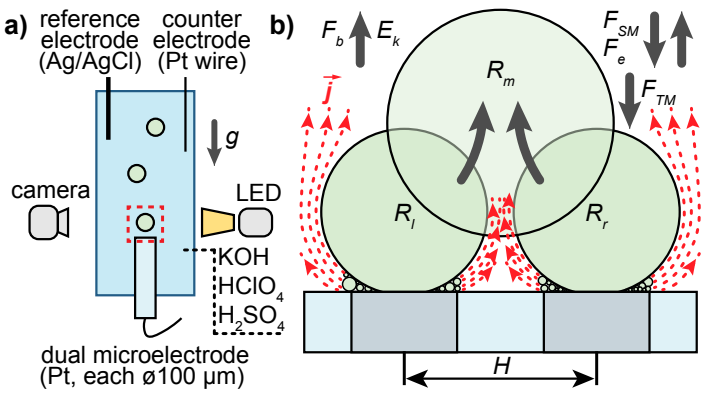

Figure 1 Schematics. (a) Three-electrode electrochemical cell combined with shadowgraphy setup. (b) Dual microelectrode with interelectrode distance H, showing two O_2 bubbles surrounded at their base by microbubbles. The red lines represent current density (j). During the oxygen evolution reaction, each growing bubble is subjected to a force balance including buoyancy (F_b), electric (F_e), and solutal and thermal Marangoni forces (F_{SM} and F_{TM}). The direction of F_{SM} is toward the electrodes for the oxygen bubbles in KOH and $HClO_4$, and away from the electrodes in H_2SO_4. The direction of F_e is upward in $HClO_4$ and H_2SO_4, and downward in KOH. The kinetic energy E_k released upon coalescence of the left (R_l) and right (R_r) bubbles drives the detachment of the merged (R_m) bubble from the microelectrodes. (b) adapted from Bashkatov *et al.*[30]

Bubble dynamics were assessed simultaneously with electrochemical measurements using a shadowgraphy setup, as demonstrated in Fig. 1a. The system consists of a high-speed camera (Photron FASTCAM NOVA S12) coupled to a long-distance microscope objective, providing a spatial resolution ranging from 496 pix/mm to 1212 pix/mm, depending on the magnification used, and frame rates ranging from 125 to 1000 Hz, and LED illumination (SCHOTT, KL 2500). Bubble size and the time between bubble nucleation and detachment, termed lifetime, were quantified using an in-house prepared Python image-processing routine.

Results and Discussion

Single electrode

To set the baseline, we first characterize bubble evolution during OER at a single microelectrode in $0.5\,M$ $HClO_4$. Consistent with our previous study on HER[30], OER in $HClO_4$ results in periodic nucleation, growth, and detachment of a single O_2 bubble with a characteristic lifetime T_s. Fig. 2a shows representative anodic potential traces ϕ_s over several consecutive cycles at applied current I varied from 0.025 mA to 0.150 mA, while shadowgraphs of a complete evolution cycle at $I = 0.100$ mA are presented in Fig. 2b. During each cycle, ϕ_s varies in response to the bubble size and its position relative to the electrode. Its minima, marked by black circles in Fig. 2a, coincide with the detachment of the bubble, after which a new bubble nucleates immediately. The subsequent growth of the bubble in the vicinity of the electrode leads to an increase in ϕ_s by up to ≈ 100 mV at $I = 0.100$ mA and ≈ 170 mV at $I = 0.150$ mA. Fig. 2c summarizes how the average anodic potential $\overline{\phi}_s$, the average departure radius $\hat{R}_s$ and the average lifetime $\hat{T}_s$ behave depending on I. The overline denotes the mean potential, obtained by first averaging over each complete bubble evolution cycle and subsequently over multiple cycles. The hat denotes an average of the instantaneous detachment radius and bubble lifetime over several bubble evolution cycles. Error bars represent the cycle-to-cycle standard deviation.

In detail, each cycle begins with the formation of several microbubbles, see $t = 0$ in Fig. 2b, which subsequently coalesce to form a larger single bubble ($t = 0.08$ s). This bubble continues to grow via the coalescence with smaller bubbles generated around the bubble bottom at the active surface of the electrode, and via the diffusion of the dissolved gas from the surrounding liquid phase. In contrast to what was previously observed for H_2 bubbles in H_2SO_4[30,34,46], we could not visually confirm a carpet of microbubbles in between the electrode and the bubble bottom throughout its evolution. This indicates that the carpet is either significantly thinner or that the bubble is directly in contact with the electrode surface.

In the present anodic $HClO_4$ system, the bubble detaches at $t = 15.11$ s, leading to a sharp potential drop marked by the black circles in Fig. 2a, once the upward-acting buoyancy F_b and electric F_e forces exceed the downward-acting solutal F_{SM} and thermal F_{TM} Marangoni forces retaining the bubble at the electrode. While $F_b \propto R^3$, F_e qualitatively depends on the polarity of the electric field and the interfacial charge density of the bubble (function of pH)[33]. In acidic electrolytes, with the pH below the isoelectric point (IEP is at $pH \approx 2-3$), the bubble interface is expected to be positively charged, whereas in alkaline electrolytes, with the pH above IEP, it becomes negatively charged[47,48]. Consequently, during OER, F_e is expected to be repulsive (upward) in $HClO_4$ and H_2SO_4, and attractive (downward) in KOH. F_{TM} originates from Joule heating caused by the locally elevated current density j near the bubble foot (Fig. 1b) and scales approximately with j^2/σ via Ohm's law, where σ denotes the electrical conductivity. F_{SM} arises from local ionic concentration gradients generated near the electrode during the reaction, such as H^+ accumulation in acidic electrolytes ($HClO_4$ and H_2SO_4) or OH^- depletion in alkaline electrolytes (KOH), and scales approximately linearly with j[49]. Charge transfer during the reaction along with the electroneutrality condition induces local electrolyte concentration (c) gradients near the bubble interface, which generate surface tension (γ) gradients and, therefore, Marangoni stresses along the interface. Since both the reaction-induced concentration gradients and surface tension increment $d\gamma/dc$ are electrolyte-dependent, the resulting F_{SM} during OER is downward in $HClO_4$ ($d\gamma/dc < 0$) and KOH ($d\gamma/dc > 0$), but upward in

View Article Online
DOI: 10.1039/D6FD00106H

H_2SO_4 ($d\gamma/dc > 0$)[35,36,49,50]. As previously demonstrated, the solutal Marangoni force F_{SM} dominates at the lower applied currents and the thermal Marangoni force F_{TM} at the larger ones[34,49].

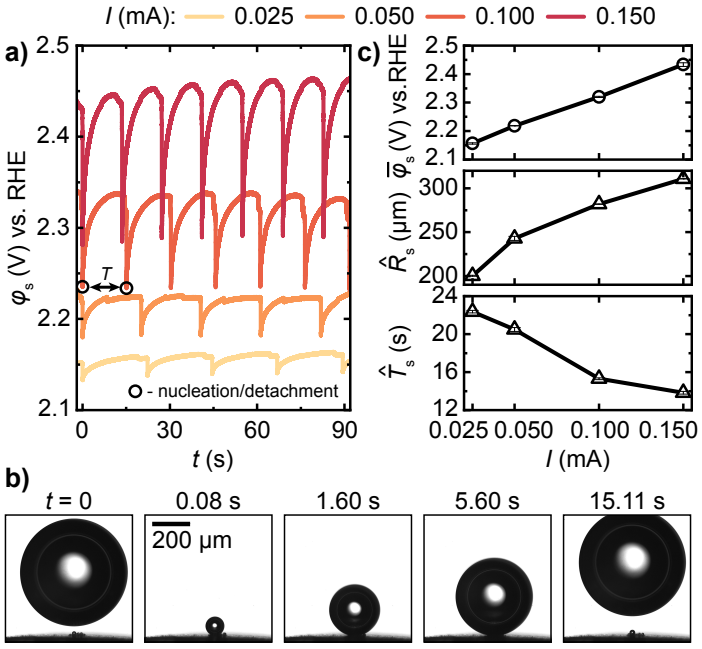

Figure 2 O_2 bubble dynamics on a single microelectrode in $0.5\,M$ $HClO_4$. (a) Potential transient (ϕ_s) at various applied currents I. (b) Snapshots during a complete bubble evolution cycle at $I = 0.100\,mA$ marked in (a). (c) Mean statistics over multiple evolution cycles: potential ($\bar{\phi}_s$), bubble detachment radius ($\hat{R}_s$), and bubble lifetime ($\hat{T}_s$). Lines are to guide the eye.

By increasing the applied current, F_{SM} and F_{TM} become stronger[33], causing the bubble to detach at larger sizes, with $\hat{R}_s = 200\,\mu m$ at 0.025 mA and $\hat{R}_s = 311\,\mu m$ at 0.150 mA, elevating the ohmic resistance and, consequently, the overpotential. In comparison, H_2 bubble evolution in H_2SO_4 yields substantially smaller detachment sizes, with $\hat{R}_s \approx 120\,\mu m$ at -0.3 V_{RHE} ($\bar{I}_s \approx -0.12$ mA) and $\hat{R}_s \approx 310\,\mu m$ at -2.3 V_{RHE} ($\bar{I}_s \approx -1.80$ mA)[30].

Because the detachment radius in Fig. 2c is set by the force balance and the bubble lifetime is $\propto R_s^3/I$ (see ref.[34]), assuming 100% gas collection efficiency, T_s decreases with increasing current. As expected from this scaling, the substantially larger O_2 bubble size together with the two-fold lower gas production rate during OER results in characteristic T_s in $HClO_4$ that are more than an order of magnitude larger than those observed for H_2 bubble evolution in H_2SO_4[30].

Finally, at currents typically above 0.150 mA (corresponding to a geometric current density $j_{geo} \approx 1.9$ A/cm^2), depending on the specific electrode sample, the single electrode configuration fails to maintain stable periodic bubble evolution (see Fig. S2a†). Because the downward-acting forces increase at higher currents, the bubble is pressed more strongly against the electrode, increasing the electrode coverage. Thus, the measured potential rapidly rises to maintain the imposed current. In addition, such electrochemical stress may alter the Pt surface through the formation of stable oxide layers, changes in surface morphology, and potentially transient Pt dissolution between bubble evolution cycles[51].

Dual electrode

Now that we have introduced the buoyancy-induced detachment at a single microelectrode, we move onto the dual electrode configuration to examine how the neighbouring bubble evolution influences the anodic potential (under galvanostatic conditions) and current (under potentiostatic conditions).

Fig. 3a shows representative potential traces $\phi_d(t)$ for the dual electrode with $H = 129\,\mu m$ over a wide range of applied currents in $0.5\,M$ $HClO_4$. The traces from the second channel (electrode) are nearly identical and are therefore omitted for clarity (see Fig. S3†). Similar to the single electrode case, demonstrated for this specific electrode in Fig. S2a†, $\phi_d(t)$ undergoes highly periodic oscillations associated with the bubble evolution cycle, exemplarily shown at $I = 0.10$ mA in Fig. 3b (see also Movie S1†). In this configuration, two O_2 bubbles grow simultaneously, each at its own electrode. Since the buoyancy-induced detachment radius (see Fig. 2c) exceeds half of the electrode separation distance ($H/2$), the bubbles eventually come into contact and coalesce. Upon coalescence, part of the released surface energy is converted into kinetic energy, driving the detachment of the merged bubble substantially earlier than would occur through buoyancy alone. Consequently, the bubble evolution cycle is interrupted before ϕ_d reaches the maximum value observed for the single microelectrode case. Also for the dual electrode, the detachment marks the onset of the subsequent bubble evolution cycle. Because the bubble size prior to coalescence is largely constrained by the electrode spacing H, the bubble lifetime T_d decreases gradually with increasing current, i.e. increasing gas production rate, from approximately 1.268 s at 0.01 mA to 0.104 s at 0.15 mA and to 0.016 s at 0.60 mA. We emphasize that the bubble lifetime T_d is substantially shorter as compared to characteristic timescale of gas production T_s, differing by approximately 1 to 3 orders of magnitude, depending on I.

View Article Online
DOI: 10.1039/D6FD00106H

To assess O_2 bubble dynamics in alkaline electrolyte and how the dual electrode configuration affects the reaction rates, we performed an additional set of experiments in 0.5 M KOH using a larger interelectrode distance $H = 242\,\mu m$ under potentiostatic conditions, consistent with our previous work[30]. The resulting current transients are shown in Fig. 3c alongside a representative bubble evolution cycle at 2.8 V_{RHE} in Fig. 3d (see also Movie S2†).

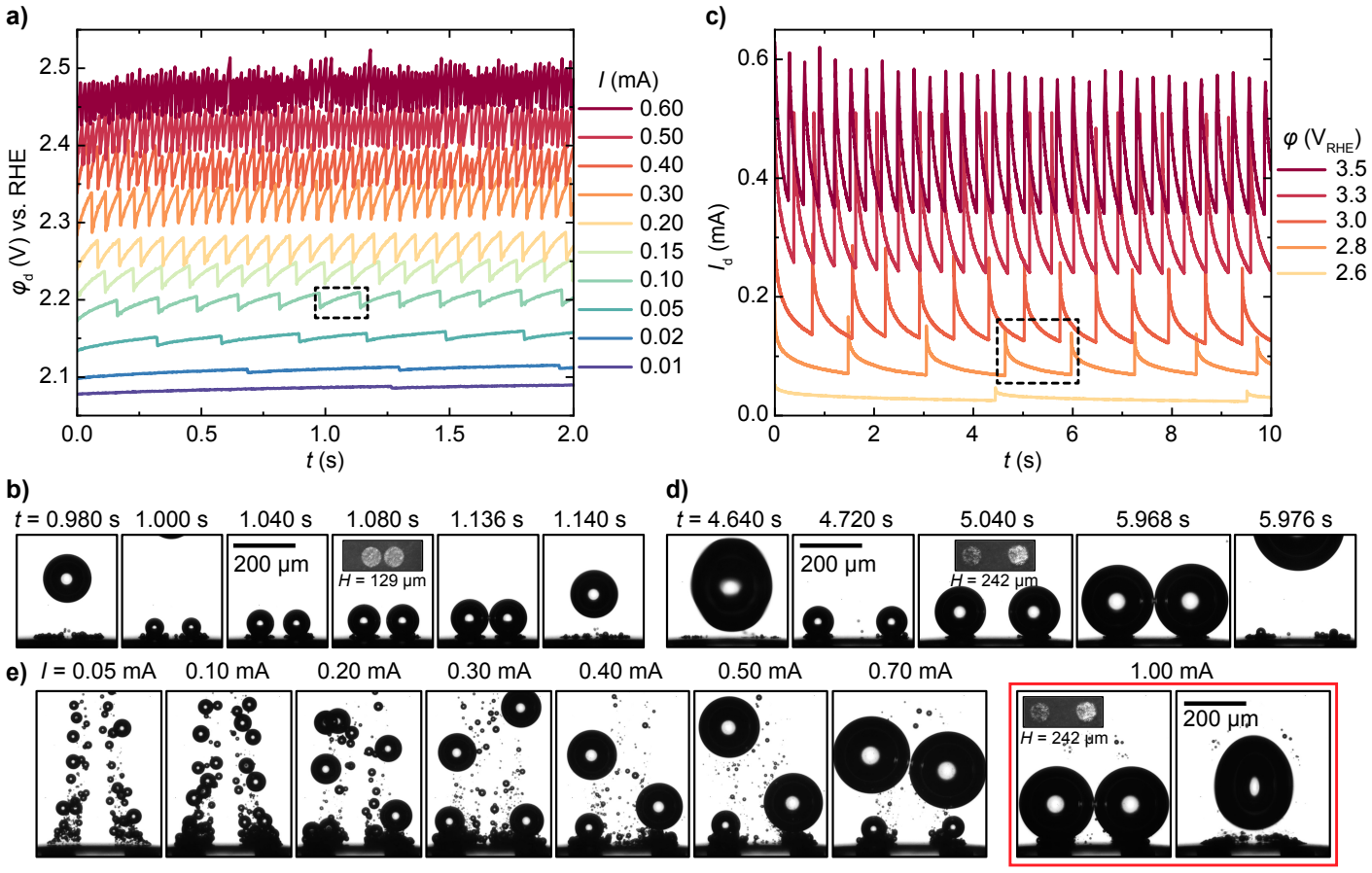

Figure 3 O_2 bubble dynamics on the dual microelectrodes. (a) Potential transients (ϕ_d) at various applied currents (I) over 2 s in 0.5 M $HClO_4$ (H =129 μm), and (b) corresponding snapshots over a complete evolution cycle at $I = 0.10$ mA. (c) Current transients (I_d) at various applied potentials over 10 s in 0.5 M KOH (H =242 μm), and (d) corresponding snapshots over a complete evolution cycle at $\phi = 2.8$ V_{RHE}. (e) Snapshots showing the bubbles at the moment of the detachment at various I in 0.5 M H_2SO_4 (H = 242 μm). Panels (a) and (c) show the data only from one of the two channels run simultaneously. Panels (b), (d), and (e) are shown at the same scale. See also Movies S1†, S2†, and S3†.

The current transients for a single electrode, shown in Supplementary Information (Fig. S2b†), demonstrate that the bubble evolution is, in principle, similar to that observed during OER in 0.5 M $HClO_4$. In particular, the bubble detachment size and lifetime are comparable in both electrolytes. Consequently, even at the larger interelectrode distance, bubble growth at the dual electrode still leads to the coalescence of two neighbouring bubbles and the subsequent detachment of the merged bubble from the electrode. The larger H increases the radius of each respective bubble required for coalescence and therefore extends bubble lifetime, which, analogous to the behavior in Fig. 3a, decreases with increasing applied potential (hence current). Under potentiostatic conditions, the current reaches its maximum at bubble detachment and, following the nucleation of the bubble successor, gradually decreases during bubble growth in response to the elevated ohmic resistance. Importantly, in contrast to HER in H_2SO_4[30,38], no comeback mode, i.e. the return of the once detached bubble back to the electrode, was observed within the studied parameter range, neither in $HClO_4$ nor in KOH. This is likely associated with the lower O_2 gas production rate during OER, which is two times smaller than that of H_2 at the same current. The growth rate of the newly formed O_2-bubbles is therefore not fast enough to catch up and coalesce with the previously departed one.

In contrast, the O_2 bubble behavior in H_2SO_4, shown for comparison in Fig. 3e (see also Movie S3†), is inherently different from that observed in both $HClO_4$ and KOH electrolytes. The snapshots in Fig. 3e show the bubbles at the moment of detachment over a wide range of applied currents for $H = 242\,\mu m$. At currents up to approximately 0.2 mA, the bubbles at each of the individual electrodes detach before they can coalesce into a single bubble. This behavior is likely associated with the different direction of the solutal Marangoni force, which during OER acts upward in H_2SO_4, thereby promoting earlier detachment, whereas in $HClO_4$ and KOH it acts towards the electrode and delays the detachment.

With increasing current, however, the downward-acting forces become progressively stronger, leading to a gradual increase in the bubble detachment size. Starting from approximately 0.3 mA, the formation and detachment of a single bubble from each electrode

View Article Online
DOI: 10.1039/D6FD00106H

become possible. Nevertheless, the detachment radius remains smaller than $H/2$, such that the system does not yet benefit from coalescence-induced detachment. Only at currents above approximately $0.7\,\mathrm{mA}$ does coalescence between neighbouring bubbles become possible, resulting in the premature departure of the merged bubble, as illustrated for the $1\,\mathrm{mA}$ case in Fig. 3e.

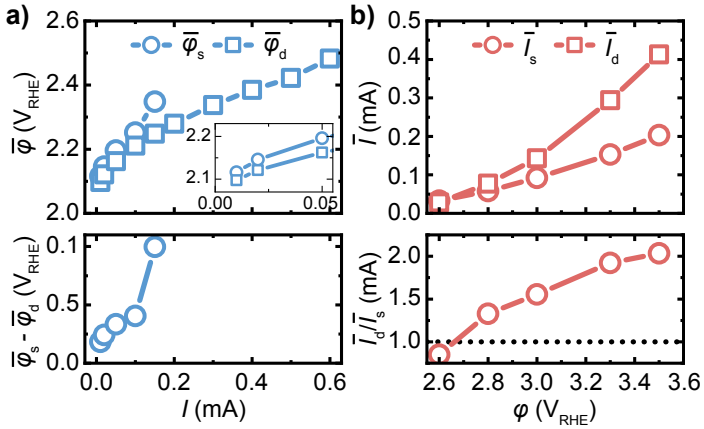

Figure 4 Electrochemical performance: dual microelectrode versus single microelectrode. (a) Mean potentials for the single ($\bar{\phi}_s$) and dual ($\bar{\phi}_d$) microelectrodes, with an inset highlighting the first three data points, and their difference ($\Delta\bar{\phi} = \bar{\phi}_s - \bar{\phi}_d$) as a function of applied current I in $0.5\,\mathrm{M}$ $HClO_4$ ($H = 129\,\mu\mathrm{m}$). (b) Mean currents for the single ($\bar{I}_s$) and dual ($\bar{I}_d$) microelectrodes and their ratio ($\bar{I}_d/\bar{I}_s$) as a function of applied potential ϕ in $0.5\,\mathrm{M}$ KOH ($H = 242\,\mu\mathrm{m}$). Lines are to guide the eye.

Next, we quantify the performance gains achieved during bubble evolution in the dual electrode configuration relative to a single electrode. Fig. 4 summarizes (a) the mean potential $\bar{\phi}$ as a function of applied current I in $0.5\,\mathrm{M}$ $HClO_4$ ($H = 129\,\mu\mathrm{m}$), and (b) the mean current $\bar{I}$ as a function of applied potential ϕ in $0.5\,\mathrm{M}$ KOH ($H = 242\,\mu\mathrm{m}$), for the single (circles) and dual (rectangles) electrode configurations. The second panels in Fig. 4(a,b) show the potential difference between single and dual electrode configurations ($\Delta\bar{\phi} = \bar{\phi}_s - \bar{\phi}_d$), and the current ratio ($\bar{I}_d/\bar{I}_s$), respectively. The overline denotes the mean potential averaged over complete bubble evolution cycles. For single electrode operation, as explained in the context of Fig. 2c, this was computed as the mean of individual cycle-averaged values over 2–6 cycles, depending on the conditions. For dual electrode operation, a simple time average over a 10 s window was used instead, since the cycle periods were sufficiently short relative to this window, containing ~2–600 cycles depending on the conditions. The values were additionally averaged over the two electrodes.

Overall, coalescence-induced detachment improves the electrochemical performance under both galvanostatic and potentiostatic conditions. In $0.5\,\mathrm{M}$ $HClO_4$, the potential difference $\Delta\bar{\phi}$ shown in Fig. 4a increases from ≈ 20 mV at 0.01 mA to ≈ 100 mV at $I = 0.15$ mA. This progressive enhancement originates from the increasing bubble size, and thus bubble-induced overpotential, at the single electrode with increasing current. In contrast, in the case of dual electrode, the bubble size is largely constrained by H, such that increasing current primarily promotes faster growth, coalescence, and earlier detachment. At $I = 0.15\,\mathrm{mA}$, the single electrode approaches a critical stability threshold, discussed in the context of Fig. 2, where the growing bubble blocks most of the electrode area due to the strong downward-acting forces. As a result, the potential response becomes less stable and attains larger magnitude, leading to reduced cycle-to-cycle reproducibility and an increased standard deviation. Beyond $0.15\,\mathrm{mA}$, the single electrode fails to maintain stable and periodic bubble evolution. By contrast, the dual electrode configuration extends the operating window and remains stable up to at least $0.60\,\mathrm{mA}$ due to the timely removal of the gas bubbles from the electrode which additionally improves mass transfer near the electrode. Importantly, the dual electrode operated at $0.30\,\mathrm{mA}$ induces a lower $\bar{\phi}_d$ than the single electrode at $0.15\,\mathrm{mA}$, despite the intrinsically higher activation overpotential at the larger current.

When operated under potentiostatic conditions in KOH, the dual electrode in Fig. 4b demonstrates a consistent enhancement of the reaction rate, reaching up to $\bar{I}_d/\bar{I}_s \approx 2$ at $\phi = 3.5$ V_{RHE}. The ratio $\bar{I}_d/\bar{I}_s$ below unity at $\phi = 2.6$ V_{RHE} can be attributed to the relatively slow bubble growth at the dual electrode, where the combined shielding effect of the two neighbouring bubbles results in a larger ohmic resistance than for a single electrode. At higher ϕ, however, the benefits of accelerated gas removal outweigh these effects. This trend closely resembles that previously reported for HER in H_2SO_4 [30].

Performance vs Interelectrode Distance, H

Before going into the details on how the anodic overpotential varies with the interelectrode distance, we first examine the dependence of the departure radius ($\hat{R}_d$) on H in Fig. 5a (see also Fig. S4†). Since bubble departure is driven by coalescence, $\hat{R}_d$, averaged over all currents represented in Fig. 5b, is primarily set by and increasing with H, consistent with our previous observations for H_2 bubbles in H_2SO_4 [30]. The dotted line therefore denotes the expected geometric limit for the $\hat{R}_d$, given by $1/2 \cdot H \cdot 2^{1/3}$, assuming two bubbles prior to the coalescence grow at the microelectrode centers. Minor deviations from this prediction are likely caused by slight electrode inclination and lateral movement of the bubbles. However, as will be shown later in Fig. 6, this limit does not necessarily hold at higher currents. Once H exceeds twice the single electrode detachment radius, each of the two bubbles will detach due to buoyancy before coalescence can occur, as illustrated for O_2 bubbles in H_2SO_4 in Fig. 3e. The maximum $\hat{R}_d$ is therefore limited to $2^{1/3} \cdot \hat{R}_s$, and indicated in Fig. 5a by the solid line using $\hat{R}_s$ measured for the electrode with $H = 242\,\mu\mathrm{m}$ at $0.01\,\mathrm{mA}$. Compared to the single electrode (grey symbols), the anodic potential in Fig. 5b is most reduced at high applied currents and small H, where the reduction in bubble departure size is maximal.

View Article Online
DOI: 10.1039/D6FD00106H

Although the smaller spacing $H = 103\,\mu m$ leads to smaller detachment radius, the electrode with $H = 129\,\mu m$ exhibits a lower potential even immediately after bubble detachment, see inset illustrating potential traces at $I = 0.10$ mA, when bubble shielding is minimal. This indicates that the improved performance of this sample ($H = 129\,\mu m$) is not governed solely by bubble dynamics, but also reflects a lower intrinsic overpotential, likely associated with differences in electrode surface roughness, effective active area, or oxide-layer-induced surface modification. Additionally, at very small interelectrode distance, such as $H = 103\,\mu m$, overlapping concentration depletion zones may reduce performance by limiting mass transport to the neighbouring electrodes.

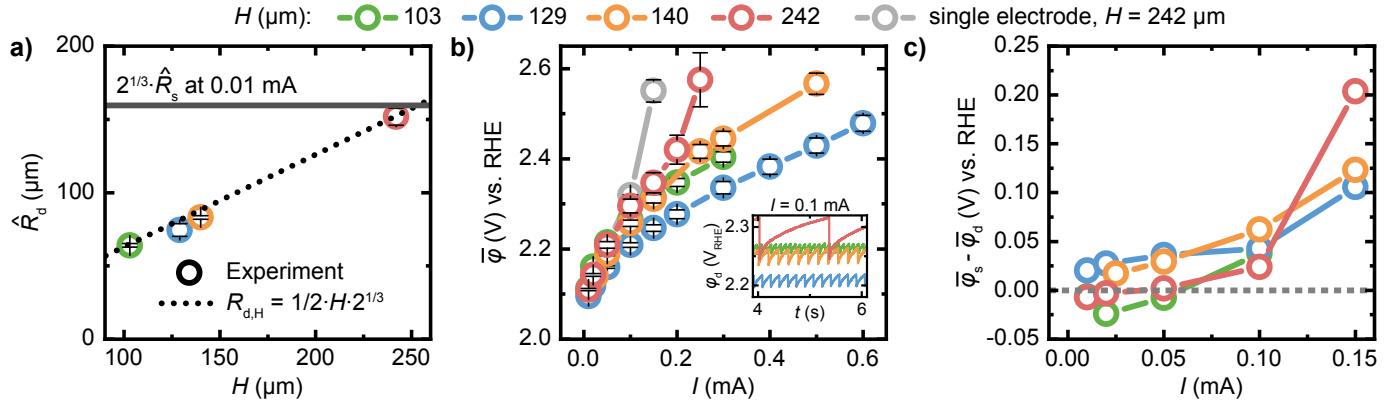

Figure 5 Electrochemical performance in 0.5 M $HClO_4$ versus *H*. (a) Mean detachment radius $\hat{R}_d$ as a function of H. (b) Mean potential $\overline{\phi}$, and (c) difference in mean potentials between single and dual microelectrode configurations, $\Delta\overline{\phi} = \overline{\phi}_s - \overline{\phi}_d$, as a function of I for various H. The inset in (b) plots the potential transients ϕ_d over a 2 s interval at $I = 0.10$ mA. Lines are to guide the eye.

To quantify the performance gain induced by premature bubble detachment, as well as to compensate for the potential dependence on the applied current and to account for the differences between dual microelectrode samples activity, we next examine the potential difference between single and dual microelectrodes $\Delta\overline{\phi} = \overline{\phi}_s - \overline{\phi}_d$. In Fig. 5c, $\Delta\overline{\phi}$ is plotted for various H as a function of I. Note that this comparison is necessarily constrained to the current range stability limit (≈ 0.15 mA) of the single microelectrode, discussed in the context of Fig. 2. Thus, the performance benefits at higher currents cannot be quantified for lack of a suitable reference.

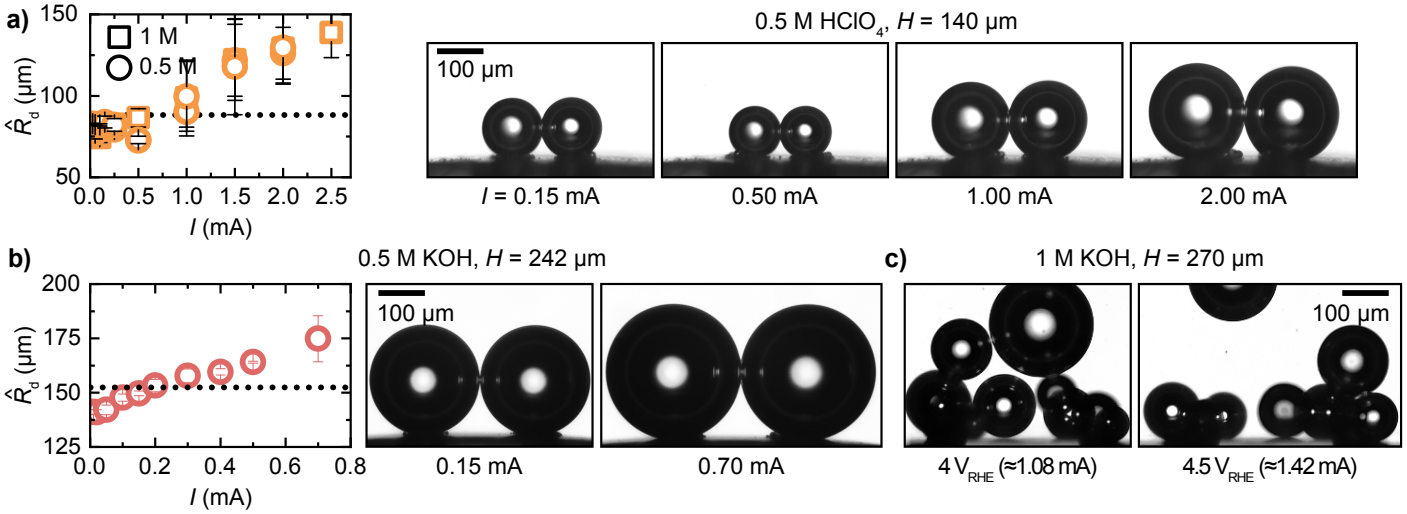

Figure 6 Coalescence inhibition. Mean detachment radius $\hat{R}_d$ as a function of I (a) in 0.5 M and 1.0 M $HClO_4$ ($H = 140\,\mu m$), and (b) in 0.5 M KOH ($H = 242\,\mu m$), along with snapshots of bubble pairs one frame prior to coalescence. (c) Snapshots in 1.0 M KOH ($H = 270\,\mu m$). All snapshots are shown at the same scale. See also Movie S4†.

Despite the much faster gas removal, the electrochemical response at low currents ($I \leq 0.05$ mA) does not necessarily improve in dual operation compared to the single electrode case[30]. For example, at $H = 103\,\mu m$ and $I = 0.02$ mA, $\Delta\overline{\phi} \approx -25$ mV indicates that elevated shielding by the neighboring bubbles, and thus the larger ohmic resistance, together with diffusive competition between closely spaced reaction sites, outweigh the benefit of earlier coalescence. In addition, the smaller bubbles produced in dual operation generate weaker effective buoyancy, resulting in reduced bubble-induced mass transfer[52]. On the other hand, placing the electrodes too far apart, e.g. $H = 242\,\mu m$, does not benefit either, as it prolongs the bubble growth before coalescence occurs, with $\hat{R}_d$ approaching that of a single electrode $\hat{R}_s$, see black line in Fig. 5a. This behavior, however, changes with increasing current. Since $\hat{R}_d$ is mostly constrained by H, the

View Article Online
DOI: 10.1039/D6FD00106H

bubbles detach progressively faster with increasing I, whereas the bubble size continues to increase for a single electrode. Consequently, $\Delta\overline{\phi}$ gradually increases, reaching approximately 100-200 mV at $I = 0.15$ mA, depending on H.

Finally, it is worth noting that at sufficiently high currents, beyond the stability threshold of a single microelectrode, neighbouring bubbles cease to coalesce efficiently in both $HClO_4$ and KOH electrolytes. This behaviour is first illustrated for $HClO_4$ ($H = 140\,\mu m$) in Fig. 6a, where $\hat{R}_d$ is plotted as a function of I together with representative snapshots of the bubble pair one frame before their coalescence.

At low currents, $\hat{R}_d$ remains below the expected coalescence limit given by $1/2 \cdot H \cdot 2^{1/3} \approx 88\,\mu m$ (dotted line), discussed in the context of Fig. 5a. However, upon current increase, $\hat{R}_d$ gradually rises reaching $\approx 139\,\mu m$ at 2.5 mA, suggesting progressively delayed coalescence. Under these conditions (see Movie S4†), the bubbles remain at their respective electrodes and appear to repel each other, thereby slowing film drainage and postponing coalescence. Measurements in 0.5 M and 1 M $HClO_4$ further suggest that this coalescence inhibition is largely independent of electrolyte concentration.

A qualitatively similar behaviour is observed in both 0.5 M (Fig. 6b and Movie S4†) and 1 M KOH (Fig. 6c). However, above a critical $I \approx 1$ mA, coalescence inhibition becomes sufficiently strong that neither electrode can sustain the formation of a single merged bubble, see Fig. 6c. Further increase in current intensifies this effect, causing the bubbles to remain in contact for longer and to behave as a coupled aggregate, as also shown in Movie S4†. We further noticed a strong downward attraction toward the electrode surface, enhancing at larger currents, likely driven by combined solutal and thermal Marangoni effects.

Conclusions

Coalescence between neighbouring bubbles can induce premature departure of the merged bubble, reducing its size and lifetime compared to buoyancy-driven detachment. This mechanism was previously shown to enhance HER performance in dual microelectrode system in H_2SO_4[30,37,38] and OER in KOH[40]. In this work, we have further extended this concept to explore the coalescence-induced dynamics of O_2 bubbles in both acidic and alkaline electrolytes by combining optical imaging with electrochemical measurements. We elucidate how the applied current or potential, electrolyte composition, and interelectrode distance H in dual operation mode affect the cell performance relative to a single microelectrode case.

During OER at a single microelectrode, O_2 bubbles in both $HClO_4$ and KOH were found to reach substantially larger detachment sizes, even at low currents, with lifetimes exceeding those of H_2 bubbles in H_2SO_4 by more than an order of magnitude. This behaviour can be rationalised by stronger downward-acting solutal Marangoni force, which increases with applied current. Consequently, progressive bubble coverage increases the anodic overpotential and limits stable periodic operation of a single microelectrode to $I \approx 0.15$ mA. In contrast, dual operation enables coalescence-induced detachment, reducing the bubble lifetime by one to three orders of magnitude, with a detachment size largely set by interelectrode distance. Through this timely bubble removal, the dual electrode configuration lowers the anodic overpotential by up to 100-200 mV under galvanostatic conditions, depending on the operating parameters, or enhances the reaction current by up to a factor of two under potentiostatic conditions. Furthermore, it enables stable operation at currents up to at least ≈ 0.6 mA (corresponding to a geometric current density $j_{geo} \approx 7.6$ A/cm^2). In contrast, O_2 bubbles in H_2SO_4 detach before a single bubble can form at low currents, whereas at higher currents they depart before coalescence occurs, thus preventing coalescence-induced benefits. This behaviour is again likely governed by the solutal Marangoni force, which in this case acts upward and promotes earlier detachment.

Finally, we found that increasing current delays coalescence between bubble pairs in both $HClO_4$ and KOH, leading to substantially larger detachment sizes, the larger the stronger the current, than those expected from the interelectrode distance alone. Impressively, in KOH at currents above ≈ 1 mA, neither electrode can sustain the formation of a single bubble. Instead, multiple smaller bubbles, which cannot quickly coalesce, remain in contact and behave as a coupled-aggregate near the electrode surface. The mechanism behind this coalescence inhibition remains open and is therefore left for future studies. Nevertheless, we would like to comment that purely electrocapillary effects are unlikely to be the dominant origin of this behaviour. In particular, no pronounced coalescence inhibition was observed in 1 M $HClO_4$ at a larger spacing of $H = 270\,\mu m$ and $I = 1.25$ mA, despite the very high anodic overpotential ($\approx$ 10 V) associated with nearly complete bubble coverage of the electrodes. Other possible mechanisms include concentration and temperature gradients, particularly strong at high currents, which may induce Marangoni stresses that alter the interfacial flow within the liquid film separating the bubbles and thereby delay its drainage[53]. In this context, the addition of surfactants or ethylene glycol during HER in H_2SO_4 was shown to inhibit bubble coalescence, likely through modifications of the interfacial stresses governing film drainage[54]. A qualitatively opposite current-dependent transition was observed during HER in $HClO_4$, where increasing potential (and thus current) promoted bubble coalescence and eventually led to the formation of a single bubble[34]. This behavior was attributed to increased collision frequency and current-induced changes in the local ionic environment that enhance coalescence efficiency. The opposite trend observed here points to fundamentally different mechanisms during OER, potentially involving reaction-induced concentration gradients and associated Marangoni stresses.

In practice, similar configurations to our dual electrode setup can be achieved on larger electrodes by designing preferential nucleation sites using, for example, hydrophobic islands[22,24,25], surface microtexturing[26,55] and laser structuring[21], or surface patterning[27] to favour coalescence-induced detachment. Such removal mechanism is also particularly relevant for microgravity applications, where buoyancy is nearly absent and coalescence-induced detachment may therefore constitute a passive gas management strategy. As demonstrated in the present work, together with previous studies, both the reaction type and electrolyte composition strongly influence bubble dynamics through the underlying force balance and should therefore be considered when designing electrodes.

Data availability

Source data of the figures are provided with this paper. See DOI: https://doi.org/10.5281/zenodo.20644855.
Supplementary information (SI): Potential and current transients for single and dual electrodes; detachment radius for single and dual electrodes; supplementary movies 1-4. See DOI: [XXX]

View Article Online
DOI: 10.1039/D6FD00106H

Conflicts of interest

There are no conflicts to declare.

Acknowledgements

D.K. received funding from NWO (The Dutch Research Council), under the VIDI grant, 'Mitigating bubble effects for highly efficient electrolysis' (project number 21305).

Notes and references

[1] N. Johnson, M. Liebreich, D. M. Kammen, P. Ekins, R. McKenna and I. Staffell, *Nature Reviews Clean Technology*, 2025, **1**, 351–371.

[2] I. Staffell, D. Scamman, A. V. Abad, P. Balcombe, P. E. Dodds, P. Ekins, N. Shah and K. R. Ward, *Energy & Environmental Science*, 2019, **12**, 463–491.

[3] G. Lopez, D. Keiner, M. Fasihi, T. Koiranen and C. Breyer, *Energy & Environmental Science*, 2023, **16**, 2879–2909.

[4] Ö. Akay, A. Bashkatov, E. Coy, K. Eckert, K. E. Einarsrud, A. Friedrich, B. Kimmel, S. Loos, G. Mutschke, L. Röntzsch *et al.*, *npj Microgravity*, 2022, **8**, 56.

[5] C. Vogt, M. Monai, G. J. Kramer and B. M. Weckhuysen, *Nature Catalysis*, 2019, **2**, 188–197.

[6] P. A. Kempler, R. H. Coridan and L. Luo, *Chemical Reviews*, 2024, **124**, 10964–11007.

[7] X. Yang, F. Karnbach, M. Uhlemann, S. Odenbach and K. Eckert, *Langmuir*, 2015, **31**, 8184–8193.

[8] A. Angulo, P. van der Linde, H. Gardeniers, M. Modestino and D. F. Rivas, *Joule*, 2020, **4**, 555–579.

[9] X. Zhao, H. Ren and L. Luo, *Langmuir*, 2019, **35**, 5392–5408.

[10] D. Walton, L. Burke and M. Murphy, *Electrochimica Acta*, 1996, **41**, 2747–2751.

[11] G. Tang, Y. Chen, J. Chen, L. Liu, H. Wen, W. Liu, J. Liu, Z. Xiao and S. Fan, *Chemical Engineering Science*, 2024, **296**, 120242.

[12] H. Rox, A. Bashkatov, X. Yang, S. Loos, G. Mutschke, G. Gerbeth and K. Eckert, *International Journal of Hydrogen Energy*, 2023, **48**, 2892–2905.

[13] J. A. Koza, S. Mühlenhoff, P. Żabiński, P. A. Nikrityuk, K. Eckert, M. Uhlemann, A. Gebert, T. Weier, L. Schultz and S. Odenbach, *Electrochimica Acta*, 2011, **56**, 2665–2675.

[14] Ö. Akay, M. Monfort-Castillo, T. St Francis, J. Becker, S. Saravanabavan, Á. Romero-Calvo and K. Brinkert, *Nature Chemistry*, 2025, **17**, 1673–1679.

[15] G. F. Swiegers, R. N. Terrett, G. Tsekouras, T. Tsuzuki, R. J. Pace and R. Stranger, *Sustainable Energy & Fuels*, 2021, **5**, 1280–1310.

[16] L. Krause, K. Skibinska, H. Rox, R. Baumann, M. M. Marzec, X. Yang, G. Mutschke, P. Zabinski, A. F. Lasagni and K. Eckert, *ACS Applied Materials & Interfaces*, 2023, **15**, 18290–18299.

[17] G. Tsekouras, R. Terrett, Z. Yu, Z. Cheng, G. F. Swiegers, T. Tsuzuki, R. Stranger and R. J. Pace, *Sustainable Energy & Fuels*, 2021, **5**, 808–819.

[18] A. Hodges, A. L. Hoang, G. Tsekouras, K. Wagner, C.-Y. Lee, G. F. Swiegers and G. G. Wallace, *Nature Communications*, 2022, **13**, 1304.

[19] P. Tiwari, G. Tsekouras, K. Wagner, G. F. Swiegers and G. G. Wallace, *International Journal of Hydrogen Energy*, 2019, **44**, 23568–23579.

[20] A. L. Hoang, R. E. Owen, G. Tsekouras, D. J. Brett and G. F. Swiegers, *Sustainable Energy & Fuels*, 2023, **7**, 4450–4460.

[21] H. Rox, F. Ranke, J. Madler, M. M. Marzec, K. Sokołowski, R. Baumann, H. Hamedi, X. Yang, G. Mutschke, L. Urbas *et al.*, *ACS Applied Materials & Interfaces*, 2025, **17**, 9364–9377.

[22] A. Raman, S. Schlautmann, H. Gardeniers and D. Fernández Rivas, *Small*, 2025, **21**, e05728.

[23] P. Peñas, P. van der Linde, W. Vijselaar, D. van der Meer, D. Lohse, J. Huskens, H. Gardeniers, M. A. Modestino and D. F. Rivas, *Journal of The Electrochemical Society*, 2019, **166**, H769–H776.

[24] O. Teschke and F. Galembeck, *Journal of The Electrochemical Society*, 1984, **131**, 1095–1097.

[25] C. Brussieux, P. Viers, H. Roustan and M. Rakib, *Electrochimica Acta*, 2011, **56**, 7194–7201.

View Article Online
DOI: 10.1039/D6FD00106H

[26] J. R. Lake, Á. M. Soto and K. K. Varanasi, *Langmuir*, 2022, **38**, 3276–3283.

[27] C.-T. Huang, L. Zheng, Y. Zhong, J. G. Werner, M.-C. Lu and C. Duan, *ACS Applied Materials & Interfaces*, 2025, **17**, 7109–7118.

[28] Ç. Demirkır, R. Yang, A. Bashkatov, V. Sanjay, D. Lohse and D. Krug, *Physical Review Fluids*, 2025, **10**, 123602.

[29] H. Matsushima, Y. Fukunaka and K. Kuribayashi, *Electrochimica Acta*, 2006, **51**, 4190–4198.

[30] A. Bashkatov, S. Park, Ç. Demirkır, J. A. Wood, M. T. Koper, D. Lohse and D. Krug, *Journal of the American Chemical Society*, 2024, **146**, 10177–10186.

[31] X. Yang, D. Baczyzmalski, C. Cierpka, G. Mutschke and K. Eckert, *Physical Chemistry Chemical Physics*, 2018, **20**, 11542–11548.

[32] J. Massing, G. Mutschke, D. Baczyzmalski, S. S. Hossain, X. Yang, K. Eckert and C. Cierpka, *Electrochimica Acta*, 2019, **297**, 929–940.

[33] A. Babich, A. Bashkatov, M. Eftekhari, X. Yang, P. Strasser, G. Mutschke and K. Eckert, *PRX Energy*, 2025, **4**, 013011.

[34] S. Park, L. Liu, Ç. Demirkır, O. van der Heijden, D. Lohse, D. Krug and M. T. Koper, *Nature Chemistry*, 2023, **15**, 1532–1540.

[35] A. Meulenbroek, N. Deen and A. Vreman, *Electrochimica Acta*, 2024, **497**, 144510.

[36] J. Haverkort, *International Journal of Hydrogen Energy*, 2024, **74**, 283–296.

[37] J. Zhang, Y. Jin, R. Tao, W. Lv and L. Chen, *Chemical Engineering Journal*, 2025, 170351.

[38] X. Zhao, Z. Duan, Y. Zeng and Q. Xu, *Available at SSRN 6838140*, 2026.

[39] X. Lu, D. Yadav, J. Liu, Z. Zeng, L. Ma and D. Jing, *Journal of Power Sources*, 2025, **632**, 236356.

[40] L. Yang, X. Li, L. Gao, X. Huo, A. Kong, B. Liu, J. Wu, W. Li and J. Zhang, *Chemical Engineering Science*, 2025, 123120.

[41] L. Janssen, C. Sillen, E. Barendrecht and S. Van Stralen, *Electrochimica Acta*, 1984, **29**, 633–642.

[42] Y. Liu, S. Li, H. Wu and Y. Shi, *DeCarbon*, 2024, **5**, 100052.

[43] K. Toyama, R. Kanemoto, R. Misumi, T. Araki and S. Mitsushima, *Electrochemistry*, 2025, **93**, 027011–027011.

[44] R. Kanemoto, K. Hirayama, K. Toyama, T. Araki and S. Mitsushima, *Journal of The Electrochemical Society*, 2026, **173**, 064507.

[45] S. Pandey, M. de Groot, K. Ozdemir, N. Sinapova and A. Niyati, *Hydrogen glides: Bubbles in alkaline water electrolysis*, 2026.

[46] A. Bashkatov, S. S. Hossain, G. Mutschke, X. Yang, H. Rox, I. M. Weidinger and K. Eckert, *Physical Chemistry Chemical Physics*, 2022, **24**, 26738–26752.

[47] C. Yang, T. Dabros, D. Li, J. Czarnecki and J. H. Masliyah, *Journal of Colloid and Interface Science*, 2001, **243**, 128–135.

[48] M. Takahashi, *The Journal of Physical Chemistry B*, 2005, **109**, 21858–21864.

[49] S. Park, D. Lohse, D. Krug and M. T. Koper, *Electrochimica Acta*, 2024, **485**, 144084.

[50] P. K. Weissenborn and R. J. Pugh, *Langmuir*, 1995, **11**, 1422–1426.

[51] A. A. Topalov, S. Cherevko, A. R. Zeradjanin, J. C. Meier, I. Katsounaros and K. J. Mayrhofer, *Chemical Science*, 2014, **5**, 631–638.

[52] F. Sepahi, R. Verzicco, D. Lohse and D. Krug, *Journal of Fluid Mechanics*, 2024, **983**, A19.

[53] B. Liu, R. Manica, Q. Liu, Z. Xu, E. Klaseboer and Q. Yang, *Physical Review Letters*, 2023, **131**, 104003.

[54] D. Fernandez, P. Maurer, M. Martine, J. Coey and M. E. Möbius, *Langmuir*, 2014, **30**, 13065–13074.

[55] P. Lv, P. Peñas, H. Le The, J. Eijkel, A. van den Berg, X. Zhang and D. Lohse, *Physical Review Letters*, 2021, **127**, 235501.